nature geoscience

ARTICLES

PUBLISHED ONLINE: 19 DECEMBER 2016 | DOI: 10.1038/NGEO2859

An accelerating high-latitude jet in Earth's core

Philip W. Livermore[1]*, Rainer Hollerbach[2] and Christopher C. Finlay[3]

Observations of the change in Earth's magnetic field—the secular variation—provide information about the motion of liquid metal within the core that is responsible for the magnetic field's generation. High-resolution observations from the European Space Agency's Swarm satellite mission show intense field change at high latitude, localized in a distinctive circular daisy-chain configuration centred on the north geographic pole. Here we show that this feature can be explained by a localized, non-axisymmetric, westward jet of 420 km width on the tangent cylinder, the cylinder of fluid within the core that is aligned with the rotation axis and tangent to the solid inner core. We find that the jet has increased in magnitude by a factor of three over the period 2000–2016 to about 40 km yr^{-1}, and is now much stronger than typical large-scale flows inferred for the core. We suggest that the current accelerating phase may be part of a longer-term fluctuation of the jet causing both eastward and westward movement of magnetic features over historical periods, and may contribute to recent changes in torsional-wave activity and the rotation direction of the inner core.

Earth's magnetic field is generated by a geodynamo in the liquid core, in which a complex motion of electrically conducting fluid stretches and advects the magnetic field, preventing its decay. Field models based on archaeomagnetic data, geomagnetic observatory series, historical records and satellite measurements have been used to reconstruct the time evolution of the magnetic field at the core–mantle boundary (CMB), the edge of the source region, over a range of timescales[1–4]. These observation-based models have shown the dominance of an axial dipolar field associated with the persistence of four quasi-stationary high-latitude equatorially symmetric flux lobes[5,6], two in the Northern Hemisphere and two in the Southern Hemisphere, believed to be a surface manifestation of rotationally aligned convection rolls. The most recent high-resolution data from the Ørsted, CHAMP and Swarm satellite missions, along with ground-based observatory data, show that, over the past decade, the northern flux lobes over Canada and Siberia have not only been moving but accelerating[1,7]. In this article, we provide an explanation of this new observation, based on an accelerating tangent cylinder jet, that sheds light on the hidden internal dynamics of the core, and which adds to the body of evidence suggesting a marked difference in magnetic change between low and high latitudes[6,8–11].

Observations of intense high-latitude secular variation

A snapshot of the magnetic field at the CMB in 2015, alongside its time derivative (the secular variation or SV), from the CHAOS-6 geomagnetic field model[1], is presented in Fig. 1. Figure 1a,b shows the radial component of the main field on the CMB for both the northern and southern high latitudes, while Fig. 1c,d shows the associated SV. Of particular prominence within the SV is a daisy chain of patches of alternating sign (labelled A–F), arranged around the north geographic pole at about latitude 70°. The same structure of SV is present in many other observation-based models of the geomagnetic secular variation covering the past 17 years (see Methods).

The distinctive pattern of SV is caused by a westward motion of the flux lobes[7,12], situated in the regions between A (80° E) and B (120° E), between C (170° E) and D (220° E), and a weaker patch between E (280° E) and F (310° E): see also the Supplementary Movies 1 and 2 of the time evolution of the main field and its SV. As the patches of negative radial flux move, they create negative signatures in the SV at their leading edges (A, C, E) and positive signatures at their trailing edges (B, D, F). These patches are a dominant feature of the high-latitude SV, having magnitudes (at epoch 2015 of about 35 μT yr^{-1}) comparable to the maximum value of SV over the core surface. Strikingly, there is no counterpart to these patches in the Southern Hemisphere (see Fig. 1d), which shows a uniformly low secular variation. In 2001, the high-latitude SV patches were recognizable in their present form but relatively weak (about 10–15 μT yr^{-1} in magnitude; see Supplementary Fig. 1).

Between 2004 and 2016 these SV patches, required by the observational data, have notably increased in magnitude. This change is robustly seen not only in CHAOS-6, but also across a wide range of other field models, built using different data sets and employing different modelling assumptions (see Methods). The only plausible explanation for the signal appears to be that it is a signature of rapidly changing magnetohydrodynamic processes taking place in the Earth's core. It is too localized to be due to remote magnetospheric sources, and the fact it is seen only in the Northern Hemisphere and not the Southern Hemisphere makes an explanation in terms of magnetosphere–ionosphere coupling or related ionospheric currents unlikely. Furthermore, this SV signal is clearly related to the evolution of the core-field's high-latitude flux lobes close to the tangent cylinder region (see Supplementary Movie 1), and thus is most likely of internal origin. The majority of the intense SV signal is contained within spherical harmonic degrees 11–13.

Localized flow close to the tangent cylinder

The latitudinal position and extent of the northern polar SV patches suggest an intimate link to dynamics close to the tangent cylinder, whose intersection with the CMB is at latitude ±69°. The tangent cylinder separates regions of quite distinct physical processes[8,13,14], a probable cause of which is that magnetic forces fail to satisfy a certain continuity condition[15,16]. Any mismatch in the radial flux of core fluid would lead to a local convergence or divergence of

[1]School of Earth and Environment, University of Leeds, Leeds LS2 9JT, UK. [2]School of Mathematics, University of Leeds, Leeds LS2 9JT, UK. [3]DTU Space, Technical University of Denmark, 2800 Kongens Lyngby, Copenhagen, Denmark. *e-mail: p.w.livermore@leeds.ac.uk

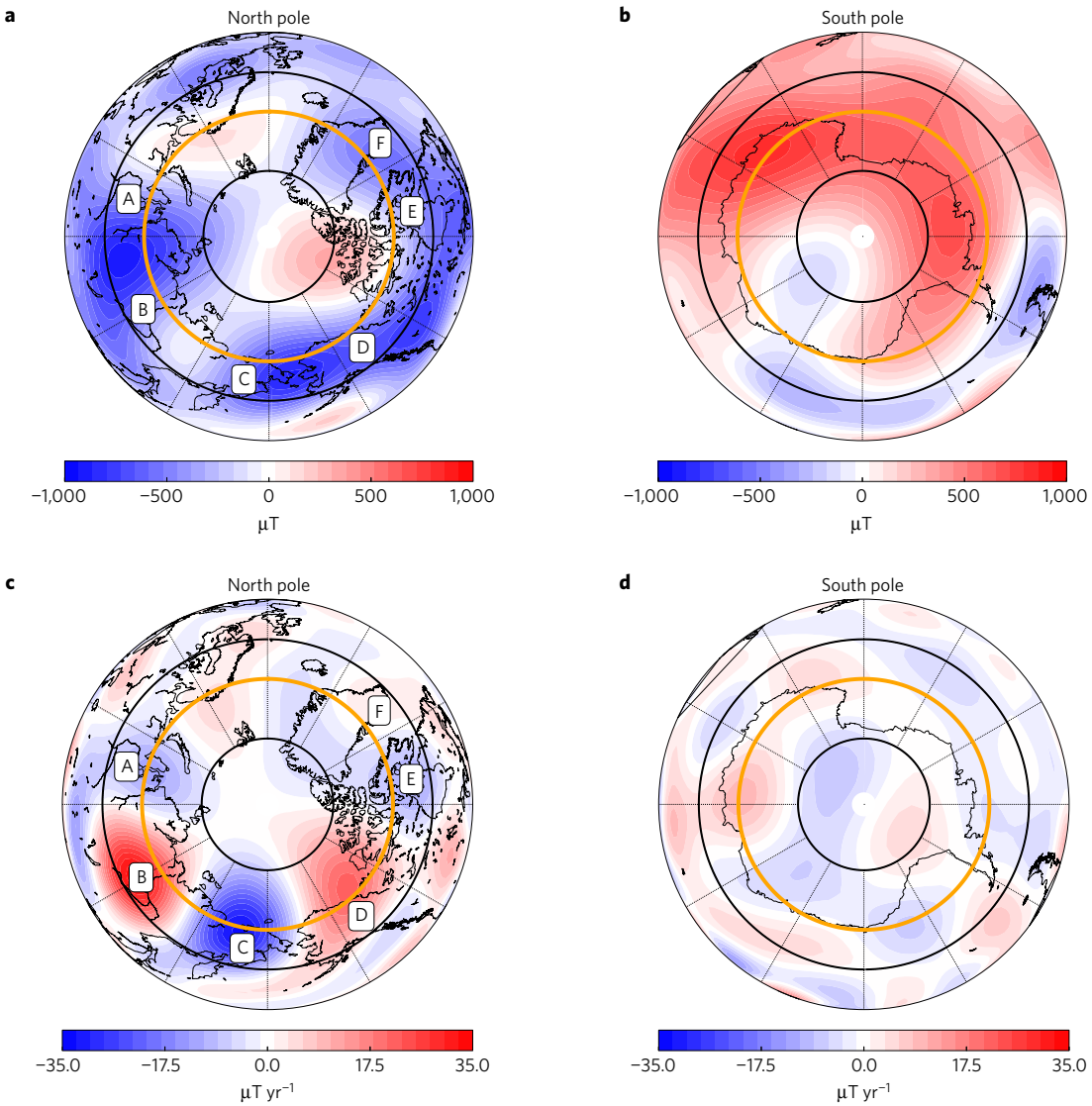

Figure 1 | Polar projection view of the radial component of the main field and secular variation at the CMB from the observation-based field reconstruction CHAOS-6 at epoch 2015. a,**b**, Map of the main field, to degree 13, for the Northern and Southern hemispheres, respectively. **c**,**d**, Map of the SV, to degree 16, for the Northern and Southern hemispheres, respectively. The tangent cylinder is shown in orange, and the lines of 60° and 80° latitude are shown in heavy weight. Features A–F label patches of SV of alternating sign.

flow, which, assuming incompressibility, would drive a lateral flow to redistribute fluid. In the rapidly rotating regime of Earth's core, this lateral flow takes the form of an equatorially symmetric jet[16] which is predominantly in the azimuthal direction and localized to the tangent cylinder. For the axisymmetric component of the jet, the need to satisfy Taylor's constraint[17] adds additional complications. Further evidence for such localized equatorially symmetric jets comes from numerical dynamo models at very low viscosity[18,19]. We therefore propose that the flow local to the tangent cylinder is a member of the well-studied class of (equatorially symmetric) quasi-geostrophic flows.

In a full-sphere geometry (neglecting the existence of the inner core), an incompressible quasi-geostrophic flow, $\mathbf{u}$, can be written in terms of a stream function Ψ in the following form[20]

$$u_s = \frac{1}{Hs}\frac{\partial \Psi}{\partial \phi}, \qquad u_\phi = -\frac{1}{H}\frac{\partial \Psi}{\partial s}, \qquad u_z = \frac{\mathrm{d}H}{\mathrm{d}s}\frac{z}{H^2 s}\frac{\partial \Psi}{\partial \phi}$$

where $H = \sqrt{1-s^2}$, (s,ϕ,z) are cylindrical coordinates and where we have non-dimensionalized length by the radius of the core (3,480 km). Provided the boundary condition $\partial\Psi/\partial\phi = 0$ at $s = 1$ is fulfilled, this flow also satisfies the impenetrable condition everywhere on the CMB.

To define a localized flow, here we define Ψ by the real part of the modal sum

$$\Psi = \sum_{m=0}^{M} a_m \mathrm{e}^{\mathrm{i}m\phi} \int_0^s \Phi_m(\rho)\sqrt{1-\rho^2}\,\mathrm{d}\rho,$$

$$\Phi_m(s) = \left[\sqrt{1-s^2}\,\mathrm{e}^{-\beta^2} - c_m\right] s^{m+1}$$

where M is the maximum wavenumber, a_m are complex coefficients to be determined, β denotes $(s-r_i)/\delta$, where r_i is the non-dimensional inner-core radius 1,221/3,480 and δ is the prescribed jet width. The constants c_m are determined through imposition of the boundary condition on each Φ_m. Each mode then has an azimuthal component proportional to $\Phi_m(s)$ which is localized to the tangent cylinder. Note that we included a factor $\sqrt{1-s^2}$, which multiplies the exponential in the definition of Φ_m, in order that Ψ could be determined analytically.

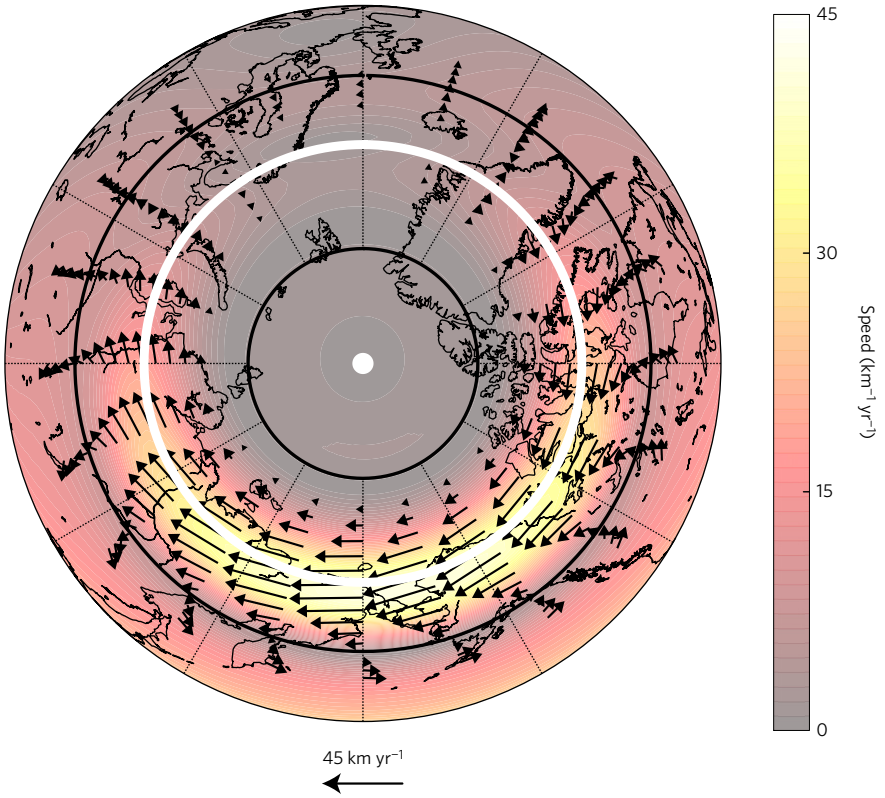

Figure 2 | Northern polar view of the flow speed and direction at the CMB of the best-fitting high-latitude jet with $M=1$ at epoch 2015. The line of 0° longitude is at the top of the figure and the tangent cylinder is marked as a thick white line. The large secular variation under Canada and Siberia can be explained by a cylindrical westwardly directed jet localized on the tangent cylinder, reaching a maximum speed of about 40 km yr^{-1}.

Observationally constrained high-latitude flow

We now investigate whether the localized SV on the CMB close to the tangent cylinder can be accounted for by such a jet. The equation that describes the rate of change of the radial field (B_r) on the core surface, under the assumption of frozen flux (that is, neglecting magnetic diffusion on account of its timescale being much longer than the interannual variations that we seek to explain), is the following

$$\dot{B}_r = -\nabla_H \cdot (\mathbf{u}_H B_r) \tag{1}$$

where $\mathbf{u}_H$ denotes the horizontal flow[21].

The tangent cylinder is located at colatitude $90 - \cos^{-1} r_i \approx 21°$, and the SV structures of interest are largely confined to 10°–30° colatitude in the north, and correspondingly 150°–170° in the south (although, as Fig. 1 shows, there is only weak SV signal in this southern region). We prescribe δ and M and fit the resulting $2M+1$ modal coefficients by minimizing the target residual defined over both northern (N) and southern (S) regions

$$\mathcal{R}_{\mathcal{N}+\mathcal{S}} = \int_0^{360°}\int_{10°}^{30°} \left(SV_{\rm obs} - SV_{\rm syn}\right)^2 \sin\theta \,\mathrm{d}\theta\,\mathrm{d}\phi + \int_0^{360°}\int_{150°}^{170°} \left(SV_{\rm obs} - SV_{\rm syn}\right)^2 \sin\theta \,\mathrm{d}\theta\,\mathrm{d}\phi \tag{2}$$

where $SV_{\rm obs}$ is the radial component of secular variation from the observational model, and $SV_{\rm syn}$ is the synthetic SV as determined from the interaction of the flow with the background field. The majority of our results are computed using the model CHAOS-6, which describes the main field at the CMB reliably to degree 13 and its associated SV to degree 16: we truncate also $SV_{\rm syn}$ to degree 16. Since the target residual $\mathcal{R}_{\mathcal{N}+\mathcal{S}}$ is quadratic in the unknown coefficients, its global minimum is straightforward to find; for each choice of M and δ a best-fitting model can be produced.

Figure 2 shows the structure of the inferred jet in 2015 defined with $M=1$, which is described by just three unknown coefficients and has associated optimal $\delta=0.12$ (in dimensional units 420 km). The jet has a maximum velocity of about 40 km yr^{-1}, twice the speed of the equatorial flux patches of 17 km yr^{-1} (ref. 9), and three times the typical r.m.s. speed of 13 km yr^{-1} from global-scale core-flow inversions[21]. This jet is confined in longitude, and so is neither circumpolar nor zonal, despite being predominantly azimuthal. A similar equatorially symmetric westward flow close to the tangent cylinder has been identified in previous direct core-flow inversions (for example, refs 22,23), and is sometimes interpreted as an integral part of a planetary-scale gyre.

Figure 3 shows the synthetic SV, along with its residual, produced by the flow of Fig. 2. The majority of the observed polar SV is described well, with the residual on a par with the background level of SV. Comparable fits are obtained for other time snapshots.

Symmetry of the flow

Although we have demonstrated that a simple non-axisymmetric and equatorially symmetric jet fits the high-latitude signal in both the Northern and Southern hemispheres, we now assess evidence for other flows that might fit the signal equally well. Table 1 shows our preferred model (row 1) alongside other models. Rows (2–3) show the effect of raising the azimuthal complexity of the jet (prescribed by M): although increases in M lower the residual (not only overall, but in both hemispheres individually), the reduction is only marginal. The residuals from all these jets are about four times smaller than that generated by zero flow (row 8).

We next consider how well axisymmetric flows can fit the data (rows 4–5), by considering not only our jet model (with $M=0$) but also that of an axisymmetric polar vortex of the form

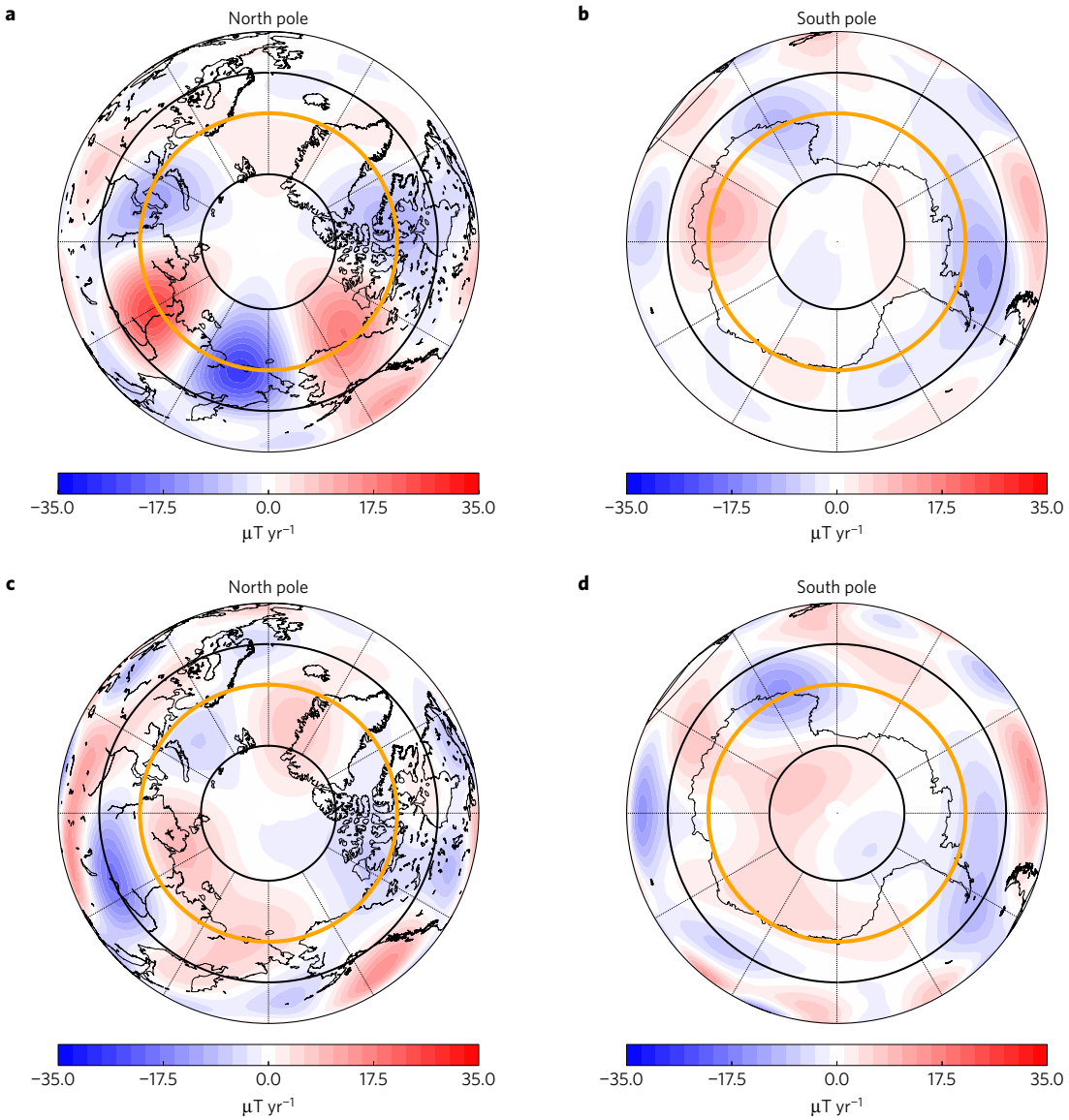

Figure 3 | Quantification of fit of the simple jet model. a,**b**, Polar projection view at the CMB of the modelled radial component of SV using a simple jet localized to the tangent cylinder for the Northern and Southern hemispheres, respectively. **c**,**d**, Residual of the modelled SV at epoch 2015 for the Northern and Southern hemispheres, respectively. The jet has a maximum azimuthal wavenumber of 1 and a non-dimensional width of $\delta = 0.12$. The tangent cylinder is shown in orange, and the lines of 60° and 80° latitude are shown in heavy weight.

$u_\phi = as + bs^3 + cs^5$, similar to that proposed in earlier studies[8,24], where the constants a, b, c were fitted by minimizing the same target residual as before. Both axisymmetric models fit the data far less well than our preferred non-axisymmetric model, principally because they predict large SV under Greenland (caused by the westward advection of a nearby flux lobe) which is absent from the observed SV signal. Thus, the higher level of detail now available in the tangent cylinder region appears to favour non-axisymmetric over axisymmetric flow structures.

Lastly, we assess whether or not the SV signal provides evidence for a jet that is equatorially asymmetric (that is, different in the Northern and Southern hemispheres), by restricting the target residual to include only one hemispheric polar region. Row 6 shows the fit of an $M = 1$ (equatorially symmetric) jet using only the signal from the north. The residual is only slightly lower in the northern polar region than our preferred model of row 1, and only slightly greater in the southern polar region, demonstrating that the southern signal lies predominantly in the null space of the inversion. Performing a similar exercise and fitting a jet using

Table 1 | A comparison of residuals produced by a variety of flow models: our preferred model is shown in row 1.

Type	Fitting region	$\mathcal{R}_N$	$\mathcal{R}_S$	$\mathcal{R}_{N+S}$
$M=1$ jet	N + S	16.8	14.2	30.9
$M=2$ jet	N + S	16.6	13.0	29.7
$M=6$ jet	N + S	14.4	11.9	26.3
$M=0$ jet	N + S	40.1	12.0	52.7
$M=0$ vortex	N + S	46.5	13.8	60.3
$M=1$ jet	N	14.8	18.8	33.6
$M=1$ jet	S	60.9	7.1	68.0
No flow	-	102.7	8.8	111.4

The model type and maximum azimuthal wavenumber M is given in column 1; the models are fitted using the target residual defined over either the northern polar region (N), the southern polar region (S) or both (N + S, see equation (2)), as shown in column 2. The integrated SV residual $\mathcal{R}$ calculated over these three regions is given in columns 3–5, expressed in units of $(\mu T\,yr^{-1})^2$. All jets have optimal width $\delta = 0.12$ correct to two decimal places. The last row shows the residuals assuming zero flow everywhere.

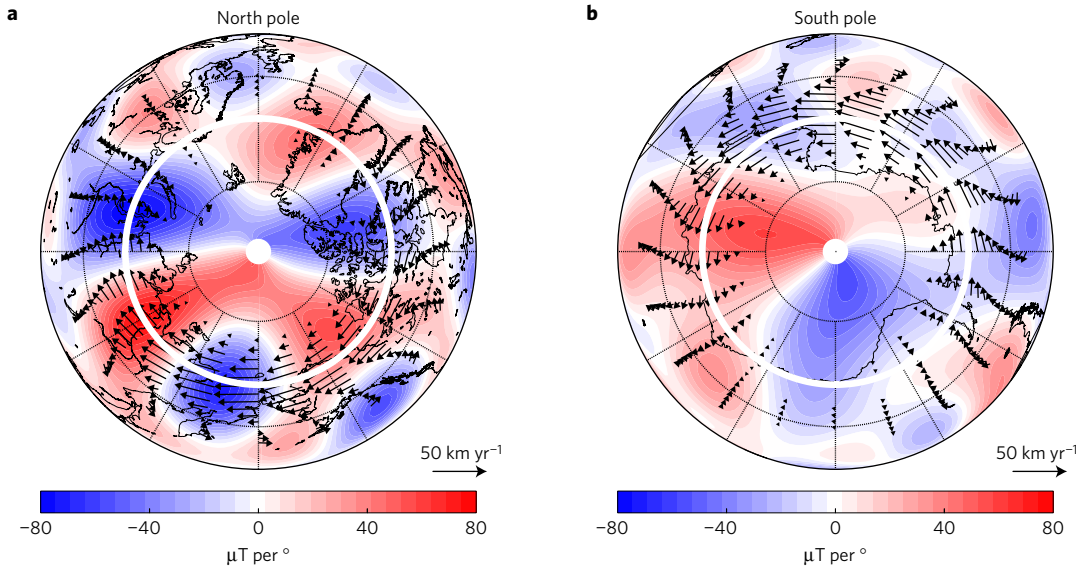

Figure 4 | A superposition of the flow direction and magnitude (arrows) and the azimuthal gradient of the radial field (in μT per °) at the CMB using CHAOS-6 at epoch 2015; together these combine to produce the SV when azimuthal advection dominates. a,**b**, In both plots the line of 180° longitude is at the bottom. In the north (**a**), the large gradients in the radial field are advected to produce a strong signature. In the south (**b**), weaker gradients in the field where the flow is strong produce comparatively little SV and the jet does not have an observable signature.

only the signal from the south leads to the residual in the south being comparable to the residual with no flow at all. Therefore, although the constraints from the northern SV signal are strong and require a jet, by contrast the southern SV signal by itself provides essentially no constraint on the flow, and serves neither to support, nor disprove, equatorial symmetry. Nevertheless, overall the data do not rule out our theoretically preferred equatorially symmetric model[16].

At first glance, it may appear surprising that our proposed equatorially symmetric jet, although strong close to the southern geographic pole, remains consistent with the small SV observed in this region (Fig. 1). To explain this, it is useful to note that if the flow is dominated by azimuthal advection rather than upwelling, then $\nabla_H \cdot \mathbf{u}_H \approx 0$ (which is the case for the optimized jets), and equation (1) simplifies to

$$\dot{B}_r = -(u_\phi \hat{\boldsymbol{\phi}}) \cdot \nabla B_r$$

where $\hat{\boldsymbol{\phi}}$ is the unit vector in the azimuthal direction. In this simple case, the secular variation is then simply longitudinal advection of the azimuthal derivative of the radial field. The importance of this effect will become clear from Fig. 4, which shows a superposition of the jet structure with the azimuthal derivative of the radial field in both the Northern and Southern hemispheres. In the north, stronger azimuthal gradients in the radial field are advected, producing the stronger patches of SV. In the south, the gradient of the radial field is relatively weak, and thus advection by a strong flow produces little SV.

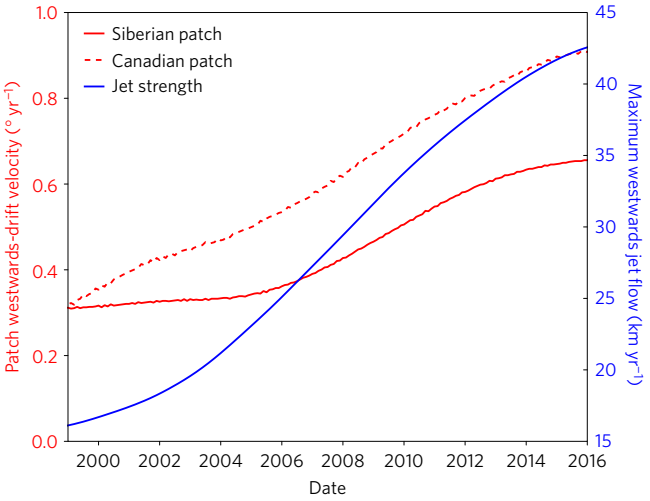

Figure 5 | Time dependence of the jet and drift of high-latitude flux patches. The maximum westward velocity of the jet (blue, right axis) of maximum wavenumber 1 and width 0.12 has increased in strength over 2000–2016 by nearly a factor of three. Also shown is the time dependence of the centre point of the Siberian (about 100° longitude, solid red) and Canadian (about 200° longitude, dashed red) high-latitude flux patches, which have also increased in westward speed by a similar factor. The centre points were determined by the location of the local minimum of radial magnetic field at the CMB according to the CHAOS-6 model to degree 13.

An accelerating jet

We are also able to explain the increasing magnitude of the high-latitude northern SV signal by considering a jet with the same $M = 1$ structure, which we now allow to vary in time. Figure 5 shows the maximum jet velocity over the period 1999–2016, which for reference is compared to the westward velocity of the centre point of the Siberian (solid red line) and Canadian (dashed red line) flux patches. These can be thought of as simple tracers for the flow, although their location does not coincide with the maximum flow speeds and the inferred flow fits the changes in the structure of the flux patches as a whole. Although the Canadian patch shows an almost uniform westward acceleration, the Siberian patch moved westwards at 0.3° yr^{-1} until 2006, when it began a westward acceleration. By 2016, both flux patches had increased in speed by a factor of 2–3. The magnitude of the jet model parallels this time dependence, being relatively weak (15–20 km yr^{-1}) until 2004, when it began a steady acceleration to a maximum speed of 40 km yr^{-1} in 2016. Supplementary Fig. 2 shows that other observation-based field models and various choices of truncation level also indicate an acceleration of the tangent cylinder jet.

The westward movement of the northern flux lobes bears some resemblance to the westward-moving flux patches on the equator[9].

However, the equatorial patches are not accelerating, and probably have a different explanation from those at high latitude—either steady advection[19,25] or wave motion[26].

Implications for core dynamics

Because the jet may ultimately result from an imbalance in fluid transport across the tangent cylinder, changes in its magnitude may reflect alterations in the dynamics on either, or both, sides of the tangent cylinder, on decadal timescales. Because inertia and viscosity are so small in the core, this would have to come about either through changes in the internal structure of the magnetic field or through changes in the fluid buoyancy distribution. Decadal changes in composition or temperature driving changes in buoyancy may be possible during an intense upwelling event. However, changes in the interior magnetic field seem to be a more likely explanation, as it is well known that the surface field, at least, changes on such timescales. Indeed, a recent model[19] has shown that altering the $l = 3, 4$ harmonics of a magnetic field (mimicking changes over centennial timescales) can not only alter the torque on the inner core, but cause significant change to the tangent cylinder jet structure and direction. Higher harmonics are expected to change faster, hence it is likely that decadal changes in the structure of the jet can be driven through internal changes in the magnetic field.

The strength and magnitude of the jet is sensitive to the sign and magnitude of the force imbalance and not the forces themselves: consequently subtle changes in the structure of the magnetic field could be enough to cause large fluctuations in the jet and its associated SV. If so, the present dynamics on the tangent cylinder is likely to episodically repeat and reverse, as the internal field changes over time. Evidence of such a westward–eastward wobble of the Canadian flux lobe[12] can be seen in the historical model *gufm1* (see Supplementary Movie 3), which shows eastward motion during 1730–1800, and westward motion during 1900–1960; there are also indications of east–west oscillations of the flux lobes on longer (centennial) timescales[27]. We suggest that we are currently observing the accelerating phase of such a wobble. This adds to the evidence for distinctive SV at high latitude[10,11], although the visibility of the jet within the SV relies on there being an appropriate structure of radial field to advect. Because the jet flow is dominantly in the azimuthal direction, it would probably not be affected by outer-core stratification[28].

Changes in the magnitude of the jet will also have repercussions for the dynamics deep within the core. Large-scale changes in axisymmetric core-flow affect the net angular momentum of the core, and therefore of the mantle; however, the jets we computed have a significant non-axisymmetric component, and therefore do not have a simple signature in change in length of day. Nevertheless, the jet will now be supplying a westwardly directed force on the inner core due to electromagnetic coupling. Interestingly, the acceleration of the jet that we find from 2004 onwards is coincident with an abrupt alteration in the rotation direction of the inner core from eastward to westward[29] that has been inferred at about the same time. Lastly, mounting evidence[30,31] suggests that torsional waves may be launched from the tangent cylinder, perhaps by the dynamics associated with the cylindrical jet[16]. An accelerating phase of the jet is consistent with independent studies[32] showing an increase in torsional-wave magnitudes over the past decade.

Methods

Methods, including statements of data availability and any associated accession codes and references, are available in the online version of this paper.

Received 6 June 2016; accepted 17 November 2016; published online 19 December 2016

References

1. Finlay, C. C., Olsen, N., Kotsiaros, S., Gillet, N. & Toeffner-Clausen, L. Recent geomagnetic secular variation from *Swarm* and ground observatories as estimated in the CHAOS-6 geomagnetic field model. *Earth Planets Space* **68,** 1–18 (2016).
2. Gillet, N., Jault, D., Finlay, C. C. & Olsen, N. Stochastic modeling of the Earth's magnetic field: inversion for covariances over the observatory era. *Geochem. Geophys. Geosyst.* **14,** 766–786 (2013).
3. Jackson, A., Jonkers, A. R. T. & Walker, M. R. Four centuries of geomagnetic secular variation from historical records. *Phil. Trans. R. Soc. Lond. A* **358,** 957–990 (2000).
4. Korte, M., Constable, C., Donadini, F. & Holme, R. Reconstructing the Holocene geomagnetic field. *Earth Planet. Sci. Lett.* **312,** 497–505 (2011).
5. Bloxham, J. & Gubbins, D. The secular variation of Earth's magnetic field. *Nature* **317,** 777–781 (1985).
6. Korte, M. & Holme, R. On the persistence of geomagnetic flux lobes in global Holocene field models. *Phys. Earth Planet. Int.* **182,** 179–186 (2010).
7. Olsen, N. *et al*. The CHAOS-4 geomagnetic field model. *Geophys. J. Int.* **197,** 815–827 (2014).
8. Hulot, G., Eymin, C., Langlais, B., Mandea, M. & Olsen, N. Small-scale structure of the geodynamo inferred from Ørsted and Magsat data. *Nature* **416,** 620–623 (2002).
9. Finlay, C. C. & Jackson, A. Equatorially dominated magnetic field change at the surface of Earth's core. *Science* **300,** 2084–2086 (2003).
10. Chulliat, A., Hulot, G. & Newitt, L. R. Magnetic flux expulsion from the core as a possible cause of the unusually large acceleration of the north magnetic pole during the 1990s. *J. Geophys. Res.* **115,** B07101 (2010).
11. Lawrence, K. *et al*. Paleomagnetic field properties at high southern latitude. *Geochem. Geophys. Geosyst.* **10,** Q01005 (2009).
12. Bloxham, J., Gubbins, D. & Jackson, A. Geomagnetic secular variation. *Phil. Trans. R. Soc. Lond. A* **329,** 415–502 (1989).
13. Hide, R. Free hydromagnetic oscillations of the Earth's core and the theory of geomagnetic secular variation. *Phil. Trans. R. Soc. Lond. A* **259,** 615–647 (1966).
14. Aurnou, J., Andreadis, S., Zhu, L. & Olson, P. Experiments on convection in Earth's core tangent cylinder. *Earth Planet. Sci. Lett.* **212,** 119–134 (2003).
15. Hollerbach, R. & Proctor, M. R. E. in *Solar and Planetary Dynamos* (eds Proctor, M. R. E. *et al*.) 145–152 (Cambridge Univ. Press, 1993).
16. Livermore, P. & Hollerbach, R. Successive elimination of shear layers by a hierarchy of constraints in inviscid spherical-shell flows. *J. Math. Phys.* **53,** 073104 (2012).
17. Taylor, J. B. The magneto-hydrodynamics of a rotating fluid and the Earth's dynamo problem. *Proc. R. Soc. A* **9,** 274–283 (1963).
18. Sheyko, A., Finlay, C. C. & Jackson, A. Magnetic reversals from planetary dynamo waves. *Nature* **539,** 551–554 (2016).
19. Livermore, P. W., Hollerbach, R. & Jackson, A. Electromagnetically driven westward drift and inner-core superrotation in Earth's core. *Proc. Natl Acad. Sci. USA* **110,** 15914–15918 (2013).
20. Labbé, F., Jault, D. & Gillet, N. On magnetostrophic inertia-less waves in quasi-geostrophic models of planetary cores. *Geophys. Astrophys. Fluid Dynam.* **109,** 587–610 (2015).
21. Holme, R. in *Treatise on Geophysics* Vol. 8 (ed. Kono, M.) 91–113 (Elsevier, 2015).
22. Pais, A. & Jault, D. Quasi-geostrophic flows responsible for the secular variation of the Earth's magnetic field. *Geophys. J. Int.* **173,** 421–443 (2008).
23. Baerenzung, J., Holschneider, M. & Lesur, V. The flow at the Earth's core mantle boundary under weak prior constraints. *J. Geophys. Res.* **121,** 1343–1364 (2016).
24. Olson, P. & Aurnou, J. M. A polar vortex in the Earth's core. *Nature* **402,** 170–173 (1999).
25. Aubert, J., Finlay, C. C. & Fournier, A. Bottom-up control of geomagnetic secular variation by the Earth's inner core. *Nature* **502,** 219–223 (2013).
26. Jackson, A. Intense equatorial flux spots on the surface of the Earth's core. *Phys. Earth Planet. Inter.* **424,** 760–763 (2003).
27. Dumberry, M. & Finlay, C. C. Eastward and westward drift of the Earth's magnetic field for the last three millennia. *Earth Planet. Sci. Lett.* **254,** 146–157 (2007).
28. Davies, C., Pozzo, M., Gubbins, D. & Alfè, D. Constraints from material properties on the dynamics and evolution of Earth's core. *Nature Geosci.* **8,** 678–685 (2015).
29. Tkalčić, H., Young, M., Bodin, T., Ngo, S. & Sambridge, M. The shuffling rotation of the Earth's inner core revealed by earthquake doublets. *Nature Geosci.* **6,** 497–502 (2013).
30. Gillet, N., Jault, D., Canet, E. & Fournier, A. Fast torsional waves and strong magnetic field within the Earth's core. *Nature* **465,** 74–77 (2010).
31. Teed, R. J., Jones, C. A. & Tobias, S. M. The transition to Earth-like torsional oscillations in magnetoconvection simulations. *Earth Planet. Sci. Lett.* **419,** 22–31 (2015).

32. Gillet, N., Jault, D. & Finlay, C. C. Planetary gyre, time-dependent eddies, torsional waves, and equatorial jets at the Earth's core surface. *J. Geophys. Res.* **120,** 3991–4013 (2015).
33. Hunter, J. D. Matplotlib: a 2D graphics environment. *Comput. Sci. Eng.* **9,** 90–95 (2007).

Acknowledgements

Swarm data used in the construction of the magnetic field models were provided by the European Space Agency. The support of the CHAMP mission by the German Aerospace Center (DLR) and the Federal Ministry of Education and Research is gratefully acknowledged. The staff of the geomagnetic observatories and INTERMAGNET are thanked for supplying high-quality observatory data. The deep-Earth research group within the School of Earth and Environment, University of Leeds, is thanked for comments and discussion on an early version of this manuscript. The figures were produced using the Python package Matplotlib[33]. The authors would like to thank R. Holme and I. Wardinski for constructive comments that helped improve the manuscript. P.W.L. was partially supported by the NERC grant NE/G014043/1.

Author contributions

All authors contributed to the design and rationale of this work. C.C.F. provided and commented on the observational field models; P.W.L. and R.H. devised the numerical scheme. P.W.L. performed the calculations and wrote the paper, on which all authors commented.

Additional information

Supplementary information is available in the online version of the paper. Reprints and permissions information is available online at www.nature.com/reprints. Correspondence and requests for materials should be addressed to P.W.L.

Competing financial interests

The authors declare no competing financial interests.

Methods

The CHAOS-6 model. CHAOS-6 is a time-dependent field model spanning 1999.0 to 2016.5 derived using magnetic field measurements made by six Low-Earth-Orbit satellites (Ørsted, CHAMP, SAC-C, and Swarm Alpha, Bravo and Charlie), as well as from 160 ground observatories. It makes use of along-track gradients of scalar and vector data from CHAMP and Swarm, as well as across-track gradients between the satellite pair Swarm Alpha and Charlie. Near-Earth magnetospheric fields and Euler angles needed for the rotation of vector data from the magnetometer frame to the geographic frame are co-estimated, and data only from geomagnetically quiet times are used. This model provides an excellent global description of recent secular variation, fitting ground observatories to a Huber-weighted r.m.s. level of 3.1 nT yr^{-1} for the eastward components and 3.8 and 3.7 nT yr^{-1} for the vertical and southward components. It has secular variation at the core surface which is stable out to at least spherical harmonic degree 16 (ref. 1). In this article, we focus on CHAOS-6 in preference to other available models because of its continuous treatment of ground and satellite data since the start of the modern era of satellite geomagnetism in 1999, its focus on high-resolution secular variation, and the generally good agreement of the CHAOS family of models with other geomagnetic reference models[34].

Robustness of the observation. In addition to CHAOS-6, the same structure of intense high-latitude SV is present in many other observation-based models of the geomagnetic secular variation covering the past 17 years. Supplementary Fig. 1 shows examples of the radial component of the secular variation at the CMB, in a polar view of the Northern Hemisphere, taken from three different models and their comparison with CHAOS-6. Along the top row is shown (i) the CM5 model[35], (ii) a recent GRIMM model, GRIMM-3[36,37], and (iii) the Swarm Initial Field Model or SIFM[38] at three illustrative epochs. Each model has a different spherical harmonic truncation, chosen to ensure that the SV remains stable at the CMB (see figure caption for details). The SV from CHAOS-6 at the same epochs and at the same truncation is also shown in the middle row for comparison; the bottom row shows the SV from CHAOS-6 truncated at degree 16.

Inspecting the top two rows, it is clear that, for each epoch, CHAOS-6 agrees well with the other models at the same resolution. Indeed, high-amplitude SV patches close to the tangent cylinder under Canada and Siberia are seen in all the models. However, differences in the magnitude of the SV are apparent (inspecting the bottom two rows) when extending the truncation to spherical harmonic degree 16. This is particularly apparent at epoch 2014.5, where the maximum SV increases from 19 μT yr^{-1} (degree 11) to 34 μT yr^{-1} (degree 16).

Robustness of jet acceleration. Here we compare CHAOS-6 to a variety of other families of observation-based geomagnetic field models, to show strong evidence for an increase in the jet magnitude over the past two decades. The families of models we compare are:

- The GRIMM series from Lesur and co-workers[36,37], from which we use a recent version, GRIMM-3. A similar algorithm using only data from Swarm was used by GFZ to produce the Swarm Level 2 Data Product: Dedicated Inversion[39]. For both models we used the SV to degree 14.
- The Comprehensive Inversion (CM) family, of which the latest published version is CM5[35]. The Swarm Level 2 Data Product: Comprehensive Inversion (CI)[39] has been produced using a similar method but using only Swarm data. For both models we used the SV to degree 13.
- The Swarm Initial Field Model (SIFM) using data only from Swarm at the single epoch of 2014.5[38]; we used the SV to degree 11.
- The POMME model series[40], of which the latest is POMME-10. We used the SV to degree 12. POMME-10 uses an alternative piecewise linear representation of the Gauss coefficients of the geomagnetic potential. It is based on vector measurements from the CHAMP satellite from July 2000 up to September 2010, total field measurements from the Ørsted satellite from January 2010 to June 2014 and vector magnetic measurements from the Swarm satellite mission from December 2013 to November 2015. It consists of main field and secular variation coefficients for each year between 2000 and 2016.
- A lower-resolution CHAOS-type model built using only data from Ørsted and ground observatories. We used the SV to degree 15.

Assuming a jet structure of $\delta = 0.12$ and $M = 1$ (as determined from CHAOS-6) we computed the best-fit jet over a set of discrete points in time (typically every 0.1 years) from 1999 onwards. For all models the main field was truncated at degree 13, but the SV truncation was chosen for each model individually to ensure that the SV power spectra at the CMB was not diverging.

The results are summarized in Supplementary Fig. 2. The POMME-10 model shows the same threefold increase in jet velocity since 2002 as CHAOS-6, although the jet strength from POMME-10 is notably more variable, probably due to its piecewise linear temporal parameterization. The strengthening jet is also supported, although to a lesser extent, by the CHAOS-type model using data from only the Ørsted satellite and ground observatories. This means that both the intensifying SV polar signal and the evidence of a strengthening jet are not consequences of the descent of the CHAMP satellite or the inclusion of recent data from Swarm. The very recent high jet strength is also supported by the single data point of SIFM with an even larger flow velocity than that inferred from CHAOS-6. The GRIMM/GFZ family, for which there is a gap in temporal coverage between 2009 and 2014.5, also shows the increase in jet velocity, although more modest than CHAOS-6. The CM5/CI family shows a constant maximum jet velocity until 2012 of about 27 km yr^{-1}, but when restricted to data from Swarm the jet velocity jumps to a value above 40 km yr^{-1}, which is comparable to that inferred from CHAOS-6. Thus, this family of field model does, overall, still support a strengthening jet.

The fact that CM5 (shown 2001–2012) shows no evidence itself for a strengthening jet seems to be related to its relatively strong regularization of secular acceleration, which will therefore also result in lower accelerations of any fitted flow. This effect is explored in Supplementary Fig. 3, which shows the SV power spectra for CHAOS-6 alongside the GRIMM/GFZ and CM5/CI families of models. Because the majority of the intense high-latitude SV patches are present in degrees 11–13, it is important that the modelling procedure allows power in this range to change. It is notable that CHAOS-6 shows the greatest temporal variability in power at high degree. The GRIMM/GFZ family shows less but still significant variability, and is largely in agreement with CHAOS-6. The CM5/CI family in contrast shows very little temporal variability in power from degree 6 upwards, as the lines defining the different epochs are almost superimposed. Therefore, it is perhaps no surprise that the jet, when fitted to this relatively temporally restricted SV, shows little variability. The independently computed CI model (using only Swarm data) shows a significant change in the shape of the SV spectra at high degree.

The families of models compared here use a range of data selection and processing methods. The fact that they all agree on an acceleration of the jet gives us confidence in our interpretation.

Code availability. The code used to generate the results shown can be obtained from the corresponding author upon request.

Data availability. Both CHAOS-6 and the SIFM geomagnetic field models can be accessed via the URL http://www.space.dtu.dk/english/Research/Scientific_data_and_models/Magnetic_Field_Models.

The GRIMM-3 model can be accessed via the URL http://www.gfz-potsdam.de/en/section/earths-magnetic-field/topics/field-models.

POMME-10 is available via the URL http://www.geomag.org/models/pomme10.html.

Information about how to access Swarm L2 products (including the field models we used) can be found at https://earth.esa.int/web/guest/swarm/data-access.

References

34. Thébault, E. *et al*. Evaluation of candidate geomagnetic field models for IGRF-12. *Earth Planets Space* **67,** 112 (2015).
35. Sabaka, T. J., Olsen, N., Tyler, R. H. & Kuvshinov, A. CM5, a pre-Swarm comprehensive geomagnetic field model derived from over 12 yr of CHAMP, Ørsted, SAC-C and observatory data. *Geophys. J. Int.* **200,** 1596–1626 (2015).
36. Lesur, V., Wardinski, I., Rother, M. & Mandea, M. GRIMM: the GFZ reference internal magnetic model based on vector satellite and observatory data. *Geophys. J. Int.* **173,** 382–394 (2008).
37. Lesur, V., Wardinski, I., Hamoudi, M. & Rother, M. The second generation of the GFZ reference internal magnetic model: GRIMM-2. *Earth Planets Space* **62,** 765–773 (2010).
38. Olsen, N. *et al*. The *Swarm* initial field model for the 2014 geomagnetic field. *Geophys. Res. Lett.* **42,** 1092–1098 (2015).
39. Olsen, N. *et al*. The *Swarm* satellite constellation application and research facility (SCARF) and *Swarm* data products. *Earth Planets Space* **65,** 1189–1200 (2013).
40. Maus, S., Manoj, C., Rauberg, J., Michaelis, I. & Lühr, H. NOAA/NGDC candidate models for the 11th generation International Geomagnetic Reference Field and the concurrent release of the 6th generation Pomme magnetic model. *Earth Planets Space* **62,** 729–735 (2010).